Acta Mech 226, 2715–2727 (2015)
DOI 10.1007/s00707-015-1347-x

ORIGINAL PAPER

Jamal Fajoui · David Gloaguen · Baptiste Girault

Modelling of elastoplastic behaviour of metallic materials with a homogenization approach: a self-consistent model based on dislocation densities

Received: 8 October 2014 / Revised: 27 February 2015 / Published online: 4 April 2015

Abstract A self-consistent scheme taking into account the intragranular microstructure is applied for the micromechanical modelling of the elastoplastic material behaviour during monotonic and sequential loading paths. The intragranular description used in the model is initially based on experimental observations of the dislocations evolution in body-centred cubic polycrystals. We have extended this description to face-centred cubic materials. For each crystallite, three internal variables are introduced to describe the microstructural features allowing to determine the mechanical characteristics of the grain. Next, a meso–macro transition using an elastoplastic self-consistent model is used to deduce the polycrystal behaviour from the grain one. A correct agreement is observed between simulations and experimental results at the mesoscopic and the macroscopic levels.

1 Introduction

Technologic progress and industrial competitiveness require complex processes of pieces fabrication. The forming processes usually involve multi-axial strain paths. Strain path changes are often limited by physical phenomena such as ductility loss, damage, strain localization, striction, wrinkling and cleavage. Those depend on both intergranular heterogeneities (texture, grain boundaries, and plastic or thermic incompatibilities) and intragranular heterogeneities (dislocation microstructure, shear microband, precipitate). Optimizing such technologies requires thus a good knowledge of the mechanical behaviour and an accurate modelling of the plastic anisotropic behaviour of deformed materials.

During elastoplastic deformation, a dislocation structure is created, and grains are broken up into cell blocks, further subdivided into cells (with low dislocation density) separated by dislocation walls (with high dislocation density) [1]. Grains present then a strong heterogeneous substructure, source of third-order internal stresses. The latter are responsible for ductility loss and material destruction.

A significant number of research works have been achieved over the last three decades in order to understand and model the dislocation structure evolution during plastic deformation. One problem met for the development of an efficient polycrystal model is the plastic anisotropy consideration and the localization of the plastic strain related to the formation of intragranular dislocation microstructure constituted of cells and walls [2–4]. The influence of this microstructure is particularly significant considering sequential loadings which are mainly used in metal forming [5]. A change in the strain path is then associated with hardening or softening effects due to the plastic anisotropy induced by the previous loading, a phenomenon already pointed out by different experimental studies [6–8]. In order to develop a relevant constitutive model, it is thus necessary to build an accurate description of the dislocation microstructure in the context of monotonic and complex paths loads.

J. Fajoui (✉) · D. Gloaguen · B. Girault
GeM - Institut de Recherche en Génie Civil et Mécanique, Université de Nantes - Ecole Centrale de Nantes -CNRS UMR 6183, 58, Rue Michel Ange, BP 420, 44 606 Saint-Nazaire, France
E-mail: jamal.fajoui@univ-nantes.fr
Tel.: +33 (0)2 72 64 87 65

So as to model the plastic deformation of a metallic polycrystal, a deductive method based on strain mechanisms and scale transition methods like Taylor [9] or self-consistent (SC) models [10] can be used. The mechanical state of the grains is considered as uniform. Consequently, the formation of the dislocation structure is neglected. These approaches allow to predict correctly the yield surface, the crystallographic texture induced by the plastic deformation, the intergranular stresses due to the initial and induced anisotropy during monotonic loadings [11,12]. Nevertheless, this kind of description fails to reproduce the mechanical behaviour during complex loading [13–15]. These methods do not, or weakly, take into account the formation, the evolution and the stability of induced dislocation microstructures which are strongly path dependent.

Over the last decades, several studies have been performed to develop models which incorporate the effects of dislocation heterogeneities on the mechanical response of a metallic material. The first attempt was proposed by Mughrabi [16] who introduced a model in which the crystal was considered as a composite material constituted with hard dislocation walls of high local dislocation density separated by soft regions of low local dislocation density. Based on Muller's works [14], the present authors [17] have extended the elastoplastic self-consistent model (EPSC) incorporating additional microstructure details at the grain scale. Two-level homogenization approaches have been developed for the micromechanical modelling of the elastoplastic material behaviour. At the microscopic level, the mechanical behaviour is described by different scale transition models like the SC approach. The grain is then considered as a two-phase material (dislocations walls and cells). The intragranular heterogeneities are highlighted by a non-local work hardening, related to the two-phase description. Next, a meso–macro transition, using the EPSC method, is applied to deduce the macroscopic response of the cubic aggregates. Simulations based on the developed model demonstrate its ability to predict the experimental response of FCC single crystals and polycrystals after moderate strain path changes.

Peeters et al. [18] have developed a semi-phenomenological crystal plasticity model that incorporates more details of the microstructural evolution at the grain scale (evolution of dislocation densities) and uses a full-constraint Taylor model in order to describe the behaviour of BCC polycrystals. Karaman et al. [19] have used a similar approach to model successfully the deformation of Hadfield steel with a viscoplastic self-consistent scheme. Viatkina et al. [20] have proposed a micromechanical model of a dislocation cell structure that accounts for the material inhomogeneity and incorporates the internal stresses in a physically based manner. A composite model was used to describe the material with its dislocation cell structure. This approach was successfully applied to predict the macroscopic behaviour of FCC alloys after various strain path changes.

In the present work, we have used the Peeters et al. [21] framework to develop an elastoplastic model that incorporates more details of the microstructure evolution at the grain scale in order to realistically reproduce the experimentally observed transients in the stress–strain responses of FCC polycrystals during strain path changes. This work concentrates on the proper understanding and modelling of the contribution of the dislocation cell structure to the strain path change effect. This microstructure modelling was coupled with a self-consistent approach to calculate the macroscopic response level (Fig. 1). In order to validate our numerical approach, a confrontation between the simulation results and those from different mechanical tests is done in two steps. Initially, the simulation accuracy is evaluated by simulating the development of intergranular strains during uniaxial loading of a Cu–Ni alloy (MONEL-400) as well as commercial purity aluminium. Neutron diffraction measurements of the elastic strains are used as a reference [22,23]. The second step involves evaluating the capability of the model to simulate the different aspects of the behaviour and the induced microstructure during complex load paths. In this respect, uni-axial Bauschinger tests in tension–compression have been carried out on AISI 316L austenitic stainless steel and aluminium alloy 6060 at room temperature.

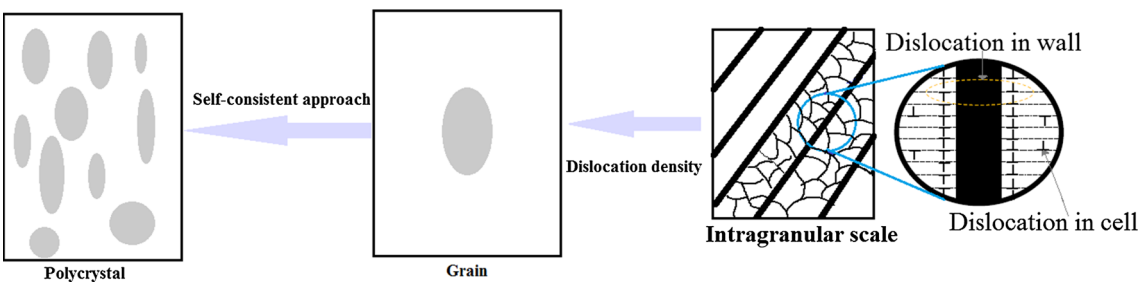

Fig. 1 Model schematization

2 The intragranular modelling

2.1 Intragranular heterogeneities description

We consider a metallic crystal with a cubic structure. We suppose that the main principal mechanism of plastic deformation is the crystallographic glide defined by slip systems. A brief description of the microstructural model is presented in this section. For more details, readers can refer to the following publications [18,21,24–26].

At the early stage of a plastic deformation process, a dislocation activity appears and is characterized by creation and mobility of dislocations along slip plans within grain. As the strain increases, dislocation microstructure develops. This structure consists of dislocation boundaries with a high lattice misorientation that envelop a number of cells to form cell blocks (see Fig. 2). The cell blocks develop in the material together with the cells and influence the macroscopic mechanical response. Based on the model of Peeters et al., this intragranular substructure (cells and walls) is described by three different types of dislocation densities introduced as internal variables in our model (Fig. 2):

- The overall dislocations stored within the cells as well as the cell boundary, i.e. cell dislocation density (ρ).
- The density of immobile dislocations (ρ^{wd}) stored in the cell block boundaries. This density parameter conveys the dislocation tangle during plastic deformation, which is responsible for latent hardening during strain path changes.
- The local directionally movable or polarized dislocation density (ρ^{wp}) in the dislocation sheet is assumed to have a polarity or sign, i.e. it can take positive and negative values. It reflects the dislocations that are immobilized on both sides of the sheet, but which can move again during reverse tests.

2.2 Formation of dense dislocation walls

In this section, we explain how dislocation walls are created and change during plastic deformation. The first task to achieve in order to apply the model is to define the dislocation walls orientations relative to the crystal lattice. The experimentally observed substructure geometry is generally complex and strongly dependent on the grain orientation and the loading direction [24].

Peeters et al. [18] assume that each grain in BCC IF steels forms dense dislocation walls parallel to the crystallographic planes on which the slip activity is the greatest, i.e. the dislocation walls have logically to belong to the {110} or {112} planes families. They find that this condition is consistent with their transmission electron microscopy (TEM) micrographies of dislocation walls. Experimentally [18,21,27,28], during the deformation, BCC material get at most two families of dislocation walls with the following criteria: the primary family of dislocation walls is generated parallel to the {110} planes of the most active slip system; the second family of dislocation walls comes out in a similar way, i.e. parallel to the {112} planes of the second active slip system. The orientation of the cell structure is logically related to the active deformation mode. The orientation of the cell walls is commonly associated with the loading axis or the slip systems activated by the applied load. In FCC single crystals, dislocation slips occur within one of the four close-packed {111} planes along one of the three <110> directions. Based on experimental observations [4,25,29] and previous results from Mahesh et al. [23], the model will develop, for each strain increment, two families of dislocation sheets parallel to the {111} planes and on which the highest and second highest slip activity rate occurs.

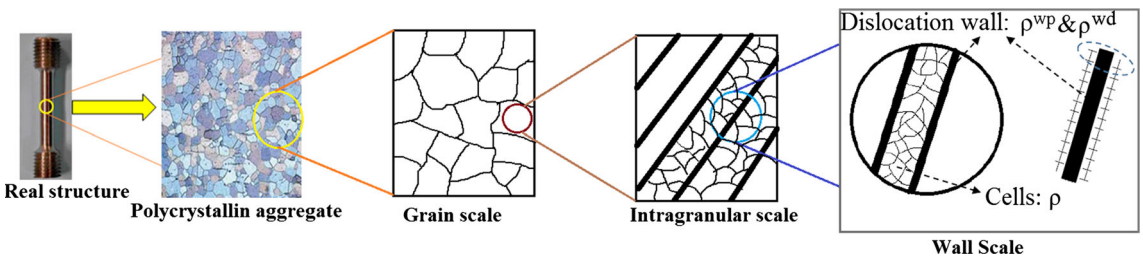

Fig. 2 Schematic representation of the dislocation microstructure. ρ represents the dislocation density inside cells; ρ^{wp} represents immobile dislocation density in walls; ρ^{wd} represents mobile dislocation density in walls

Table 1 Families of dislocation walls [21,24]

No. of dislocation walls	Family of walls
1	(111)
2	$(\bar{1}11)$
3	$(1\bar{1}1)$
4	$(11\bar{1})$

Four independent families of dislocation walls can be defined and are listed in Table 1 [24]. The intragranular heterogeneities are assimilated to families of dislocation walls, parallel to the {111} planes having their most dominants slip activities.

2.3 Dislocation density evolution

Each of the dislocation densities considered in the model has an evolution law determined using the well-known Kocks-type law [30]: the evolution of dislocation density results from the competition between production and annihilation rates of dislocations.

For FCC metals, the plastic deformation has been modelled assuming (110)<111> slip systems. As mentioned before, FCC material is characterized by four independent families of dislocation walls. n_i^w $(i = 1, 2, 3, 4)$ is the unit vector perpendicular to the existing generated dense sheet wall i and m_s $(s = 1, \ldots, 12)$, the unit vector along the slip direction of a system s. n_i^w and m_s allow to calculate two terms needed in order to determine the different dislocation densities:

- For each currently generated dislocation wall i of an increment of deformation, the net flux of dislocations is given by:

$$\Phi_i = \sum_{s=1}^{n} \frac{\dot{\gamma}_s}{b} m_s \cdot n_i^w \tag{1}$$

  where b represents the magnitude of the Burgers vector. The symbol n refers to the number of slip systems. $\dot{\gamma}_s$ is the slip rate on system s and can be positive or negative. When a slip system is coplanar with a dislocation wall, the dislocation flux Φ_i is equal to zero.
- The total slip rate on the plane of the ith most active slip system is:

$$\dot{\Gamma}_i = \sum_{s:u_s^b \cdot u_i^w = 0} |\dot{\gamma}_s|. \tag{2}$$

2.3.1 The currently generated dislocation walls

The evolution of the local density of immobile dislocations w^{d} stored in walls can be further decomposed into a storage term and a recovery term [30].

The evolution of the immobile dislocation density for each of the existing generated dislocation sheets will thus be expressed as:

$$\dot{\rho}_i^{\mathrm{wd}} = \left(I^{\mathrm{wd}} \sqrt{\rho_i^{\mathrm{wd}}} - R^{\mathrm{wd}} \rho_i^{\mathrm{wd}} \right) \frac{\dot{\Gamma}_i}{b}, \quad (i = 1, 2)\,. \tag{3}$$

I^{wd} and R^{wd} are, respectively, the storage and annihilation coefficients of dislocations.

During the plastic deformation, we observe the polarization of the dislocation walls: a mobile dislocation is stopped and stored in a wall face (with sign), and the dislocation with opposite sign is stopped and stored in the facing face. This phenomenon generates an asymmetry in the plastic slip resistance depending on the considered direction. This result explains the elastic yield difference observed between the first and the second loading (Bauschinger effect). In a reverse test, polarized dislocations move from the wall and annihilate with dislocations stored inside the cell; this explains the transitional regime observed during strain path change. With strain, these walls become polarized again, but in the opposite sign, and then the same behaviour as the pre-strain is obtained.

The storage and annihilation of polarized dislocations for each dislocation wall can be expressed by means of the summation of those (storage and annihilation):

$$\dot{\rho}_i^{\mathrm{wp}} = \left(I^{\mathrm{wp}} \sqrt{\rho_i^{\mathrm{wd}} + \left|\rho_i^{\mathrm{wp}}\right|} \ \mathrm{sign}\ (\Phi_i) - R^{\mathrm{wp}} \rho_i^{\mathrm{wp}} \right) |\Phi_i| \,. \tag{4}$$

I^{wp} and R^{wp} become, respectively, the storage and annihilation coefficients of polarized dislocations.

In a reverse test, most of the active systems during the pre-strain remain active, but operate in the opposite sense. The dislocation flux associated with a family of currently generated dense walls i is then reversed. The polarized dislocations that have already been accumulated along walls can then easily move away and be annihilated by dislocations of opposite sign, a phenomenon which can be expressed by the following equation:

$$\dot{\rho}_i^{\mathrm{wp}} = -R_{\mathrm{rev}} \rho_i^{\mathrm{wp}} |\Phi_i| \tag{5}$$

where R_{rev} is a material parameter; it goes with the rate of annihilation of the mobile dislocations responsible for the polarity of the dense dislocation walls and consistent with the reversal of the flux.

2.3.2 Non-currently generated dislocation walls

When a dense dislocation wall is not currently generated anymore, mainly due to a change of slip activity, the dense dislocation walls are supposed to disintegrate themselves. The following equations are used for the removal of the old dislocation structures:

$$\dot{\rho}_i^{\mathrm{wd}} = -\frac{R_{\mathrm{ncg}}}{\mathrm{b}} \rho_i^{\mathrm{wd}} \dot{\Gamma}_{\mathrm{new}}, \tag{6}$$

$$\dot{\rho}_i^{\mathrm{wp}} = -\frac{R_{\mathrm{ncg}}}{\mathrm{b}} \rho_i^{\mathrm{wp}} \dot{\Gamma}_{\mathrm{new}}. \tag{7}$$

$\dot{\Gamma}_{\mathrm{new}}$ is the total slip rate on both of the crystallographic planes containing the highest slip activity. R_{ncg} indicates a parameter that characterizes the destruction of former dense dislocation walls.

2.3.3 Evolution of cell dislocation density ρ

During a monotonic loading, the evolution of the dislocation density ρ is expressed by the summation of a storage term and an annihilation term:

$$\dot{\rho} = \left(I\sqrt{\rho} - R\rho \right) \frac{\sum_{\mathrm{s}} |\dot{\gamma}^{\mathrm{s}}|}{b} \tag{8}$$

where I and R are, respectively, the immobilization and the annihilation parameters.

During a reverse test, the annihilation of dislocations inside cells will be more important than their storage. This remark is valid for small strain, i.e. in the transient region of a reverse test. An additional source of annihilation is added to Eq. (8) to take into account this phenomenon and leading to the following expression:

$$\dot{\rho} = \left\langle \left(I\sqrt{\rho} - R\rho \right) \frac{\sum_s |\dot{\gamma}^s|}{b} - \Psi R_2 \rho \frac{\rho_{\mathrm{bausch}}}{\rho_{\mathrm{sat}}^{\mathrm{wp}}} \frac{\sum_s |\dot{\gamma}^s|}{b} \right\rangle \tag{9}$$

where $<x>= x$ when $x > 0$ and $<x>= 0$ otherwise. The parameter R_2 reflects the importance of the annihilation of the statistically stored dislocations within the cell by the remobilized directionally movable dislocations associated with the dense dislocation sheets. The switch parameter Ψ will activate ($\Psi = 1$) or not ($\Psi = 0$) this additional term, depending on whether there is reversal of the flux associated with a family of currently generated walls or not. The value of ρ_{bausch} will be different according to the number of reversed fluxes. In summary, if only one flux is reversed, then $\rho_{\mathrm{bausch}} = \left|\rho_i^{\mathrm{wp}}\right|$; otherwise, $\rho_{\mathrm{bausch}} = \sum_{i=1}^{2} \left|\rho_i^{\mathrm{wp}}\right|$.

3 Mesoscopic modelling

3.1 Critical resolved shear stress

The physical quantities, defined previously, are incorporated into the critical resolved shear stress (CRSS) definition. Consequently, the CRSS τ_c^g on a slip system g is composed of several contributions: (i) immobile dislocations density; (ii) polarized dislocations density, (iii) cells dislocation density, (iv) the initial critical resolved shear stress τ_{c0}^g which takes into account all other microstructural phenomena (e.g. precipitates), and (v) f, the volume fraction of the dislocation sheets:

$$\tau_c^g = \tau_{c0}^g + (1-f)\,\tau^{\text{Cell}} + f\sum_{i=1}^{4}\left(\tau_{ig}^{\text{wd}} + \tau_{ig}^{\text{wp}}\right), \tag{10}$$

with:

- τ^{Cell}, the isotropic hardening caused by the statistically stored dislocation density within the cell:

$$\tau^{\text{Cell}} = \alpha\mu \text{b}\sqrt{\rho} \tag{11}$$

  where α is the dislocation interaction parameter and μ, the shear modulus.
- τ_{ig}^{wd}, the latent hardening caused by the immobile dislocation density, stored in a family of walls i:

$$\tau_{\text{ig}}^{\text{wd}} = \alpha\mu \text{b}\sqrt{\rho_i^{\text{wd}}}\left|m_g \cdot n_i^w\right|. \tag{12}$$

- τ_{ig}^{wp}, the latent hardening caused by the dislocation wall polarity, associated with a family of dislocation walls i:

$$\tau_{\text{ig}}^{\text{wp}} = \alpha\mu \text{b}\left\langle\sqrt{\left|\rho_i^{\text{wp}}\right|}m_g \cdot n_i^w \cdot \text{ sign }\left(\rho_i^{\text{wp}}\right)\right\rangle. \tag{13}$$

3.2 Slip system activation

Plastic deformation takes place when a slip system becomes active. Slip occurs if the resolved shear stress τ^g on a system g is equal to the critical value τ_c^g and if the system remains sufficiently loaded during the stress evolution:

$$\tau^g = R^g : \sigma^{\text{II}} = \tau_c^g \quad \text{and} \quad \dot{\tau}^g = R^g : \dot{\sigma}^{\text{II}} = \dot{\tau}_c^g \tag{14}$$

where R^g is the Schmidt tensor on a system g.

A : B denotes the double scalar product $A_{\text{ijkl}}B_{\text{klmn}}$ using the Einstein summation convention. If $\dot{\gamma}^g$ denotes the slip rate on a system g, the Schmid criterion is thus given by:

$$\dot{\gamma}^g = 0 \quad \text{when} \quad \tau^g < \tau_c^g, \tag{15.1}$$

$$\dot{\gamma}^g = 0 \quad \text{when} \quad \tau^g = \tau_c^g \quad \text{and} \quad \dot{\tau}^g < \dot{\tau}_c^g, \tag{15.2}$$

$$\dot{\gamma}^g > 0 \quad \text{when} \quad \tau^g = \tau_c^g \quad \text{and} \quad \dot{\tau}^g = \dot{\tau}_c^g. \tag{15.3}$$

The main problem is to determine which combination of slip systems will actually be activated at each step of the plastic deformation path. In this case, all possible combinations of potentially active systems must be scanned in order to find one that satisfies the previous conditions (15) simultaneously. Since it has to be performed in a large deformation framework, running time considerations become one of the main problems of the model. Moreover, this method can give several equivalent solutions for some hardening matrices. Franz et al. [26] proposed a different formulation to resolve the problem of ambiguous selection of deformation systems and reduce the running time of the computations. Their numerical results in the case of BCC single crystals present a good agreement with the "classical" crystal plasticity based on the critical resolved shear stress. This formulation has been extended to the polycrystalline model framework by Lorrain et al. [31]. The accuracy of the simulations has also been evaluated at the mesoscopic and macroscopic levels thanks to

mechanical experiments (tensile tests, neutron diffraction). Based on the work of [26], the relations (15.1), (15.2) and (15.3) can be expressed by the following equation:

$$\dot{\gamma}^g = K^g(\tau^g, \tau_c^g)\dot{\tau}^g. \tag{16}$$

The slip rate is linked to the resolved shear stress rate through a function K^g. Among several possible regularization functions, the following form is adopted here [31]:

$$K^g = \frac{1}{\eta}\left[\frac{1}{2}\left(1+\tanh\left(k\left(\frac{\tau^g}{\tau_c^g}-1\right)\right)\right)\right]\left[\frac{1}{2}\left(1+\tanh\left(k\dot{\tau}^g\right)\right)\right]\left[\frac{1}{2}\left(1+\tanh\left(k\tau^g\right)\right)\right] \tag{17}$$

where η and k are numerical parameters.

Considering an additional split up of strain rate $\dot{\varepsilon}^{\mathrm{II}}$ into elastic and plastic parts, $\dot{\varepsilon}^{\mathrm{II}}$ can be written as:

$$\dot{\varepsilon}^{\mathrm{II}} = \dot{\varepsilon}^{\mathrm{eII}} + \dot{\varepsilon}^{\mathrm{pII}}. \tag{18}$$

The plastic strain rate $\dot{\varepsilon}^{\mathrm{pII}}$ is related to the tensor R^g and the slip rate $\dot{\gamma}^g$ in the system g by the expression:

$$\dot{\varepsilon}^{\mathrm{pII}} = \sum_g R^g\dot{\gamma}^g. \tag{19}$$

Using the usual generalized Hooke's law and Eq. (16), the slip rate related to a system g becomes:

$$\dot{\gamma}^g = K^g\dot{\tau}^g = K^g R^g : \dot{\sigma}^{\mathrm{II}} = K^g R^g : c : \dot{\varepsilon}^{\mathrm{eII}} \tag{20}$$

where c is the elastic constant tensor at the grain level.

After calculations, one obtains the following slip rate expression:

$$\dot{\gamma}^h = \left(\delta_{gh} + K^g R^g : c : R^h\right)^{-1} K^g R^g : c : \dot{\varepsilon}^{\mathrm{II}} = N^{hg} : \dot{\varepsilon}^{\mathrm{II}}. \tag{21}$$

3.3 Mechanical behaviour at grain level

Considering relations (18) and (21), and the usual generalized Hooke's law, the constitutive elastoplastic relationship for the single crystal can be deduced:

$$\dot{\sigma}^{\mathrm{II}} = \left(c + \sum_h\sum_g c : R^h : N^{hg} : c\right) : \dot{\varepsilon}^{\mathrm{II}} \tag{22}$$

with:

$$\dot{\sigma}^{\mathrm{II}} = \ell : \dot{\varepsilon}^{\mathrm{II}} \tag{23}$$

where ℓ is the tensor of tangent elastoplastic moduli of the single crystal written as follows:

$$\ell = c + \sum_g\sum_h c : R^g : \left(\delta_{gh} + K^g R^g : c : R^h\right)^{-1} K^h R^h : c. \tag{24}$$

4 Meso–macro transition scheme

The relation between stress and strain rates can be written for the mesoscopic scales and macroscopic scale as follows:

$$\dot{\sigma}^{\mathrm{II}} = \ell : \dot{\varepsilon}^{\mathrm{II}} \quad \text{and} \quad \dot{\sigma}^{I} = L : \dot{\varepsilon}^{I} \tag{25}$$

where L is the macroscopic tangent modulus for the fictional average homogeneous medium. ℓ corresponds to the modulus defined above. $\dot{\sigma}^{I}$ and $\dot{\varepsilon}^{I}$ are, respectively, the macroscopic stress and strain rates.

The local strain and stress rates can be obtained classically through the localization A and concentration B tensors:

$$\dot{\varepsilon}^{\mathrm{II}} = \left[I + S^{\mathrm{esh}} : L^{-1} : (\ell - L)\right]^{-1} : \dot{\varepsilon}^{I} = A : \dot{\varepsilon}^{I}, \tag{26}$$

$$\dot{\sigma}^{\mathrm{II}} = \ell : \left[I + S^{\mathrm{esh}} : L^{-1} : (\ell - L)\right]^{-1} : L^{-1} : \dot{\sigma}^{I} = B : \dot{\sigma}^{I} \tag{27}$$

where S^{esh} is the Eshelby tensor.

The averages of the local stress and strain tensors over the volume must match the overall strain and stress. Following some algebraic calculations, these conditions give access to the overall elastoplastic tensor L as a weighted average of the mesoscopic tensor l:

$$L = \left\langle \ell : \left[I + S^{\mathrm{esh}} : L^{-1} : (\ell - L)\right]^{-1} \right\rangle. \tag{28}$$

Equation (28) is a nonlinear implicit equation because S^{esh} depends on the unknown L in the framework of elastoplastic self-consistent theory. The Eshelby tensor is calculated by an integral equation [32] that takes the plastic anisotropy fully into account. This equation is solved iteratively. Once L is known, and specifying an overall stress or strain increment, the model can give the corresponding stress or strain tensors for each orientation. Therefore, the mechanical response of the polycrystal can be described.

5 Numerical results

In this section, the capability of the enhanced model to predict the mechanical behaviour of metallic polycrystals subjected to monotonic and complex load paths is verified at two scales: mesoscopic and macroscopic.

In order to perform numerical simulations, the model parameters associated with physical variables must be identified. Their values are chosen to be coherent with those given in the literature.

For FCC metals, the plastic deformation has been modelled assuming (110)<111> slip systems. Identical initial critical resolved shear–stress τ_{c0} has been chosen for each deformation mode. This CRSS is determined in order to reproduce the experimental yield stress. The values of k and η (Eqs. 17, 18) for each material have been determined comparing the experimental results with our model under monotonic loading (in terms of main active deformation systems and crystal reorientation). The immobilization parameters (I, I^{wd}, I^{wp}) and the recovery parameters (R, R^{wd}, R^{wp}, R_2, R_{rev}, R_{ncg}) have been adjusted so that the model fits properly the experimental pre-strain curve. This method of identification must be viewed with utmost caution since it can lead to several numerical solutions. Thereafter, it would be thus interesting to develop an optimization approach based on experimental and statistical analysis in order to reduce the interval of each parameter.

5.1 Prediction of intergranular strains

As a first step, the model has been used to predict the development of elastic lattice strains during monotonic uniaxial loading. Clausen and Lorentzen [22,23] have measured lattice strains in commercial purity aluminium loaded up to 3 % total strain with in situ neutron diffraction measurements. Holden et al. [9] have carried out a similar study on MONEL-400 (Cu–Ni alloy) samples during an uniaxial tensile test up to 5 % total strain. Lattice strains have been determined along the loading direction for 111 and 220 reflections. The elastic single-crystal stiffness (GPa) for aluminium (MONEL-400) is as follows [9,33]: $c_{11} = 107.3(220.8)$, $c_{12} = 60.9(148)$, $c_{44} = 28.3(107.4)$.

The initial texture is considered as isotropic and described by three randomly generated Euler's angles. Lattice rotation and thus texture changes are incorporated in the model. The model calculations were performed

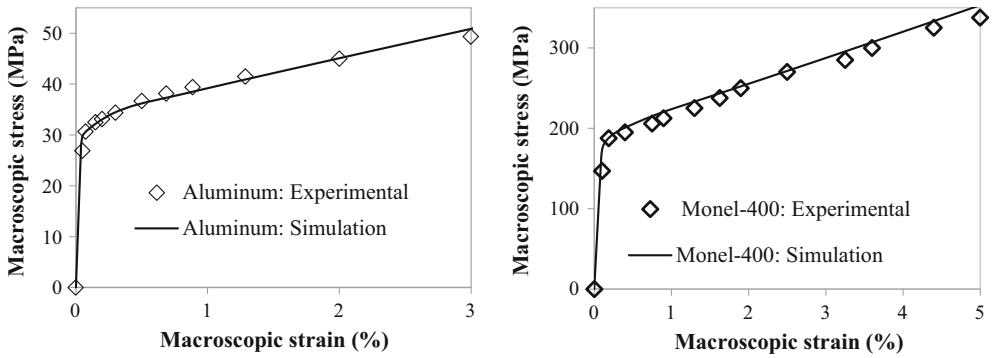

Fig. 3 Simulated and experimental macroscopic tensile curves for aluminium and MONEL-400

Table 2 Material parameters used for aluminium and for MONEL-400

τ_{c0} (MPa)	k	η	α	I	I^{wd}	I^{wp}	ρ_0 (m^{-2})	R (m)	R^{wd} (m)	R^{wp} (m)	R_{ncg} (m)	R_{rev} (m)	R_2 (m)
Aluminium													
11	0.5	150	0.1	10^{-2}	$3\,10^{-1}$	10^{-1}	10^{9}	10^{-9}	10^{-9}	10^{-9}	10^{-9}	5×10^{-9}	5×10^{-9}
MONEL-400													
69	1.7	180	0.13	0.2	3×10^{-1}	10^{-1}	3×10^{9}	5×10^{-9}	5×10^{-9}	5×10^{-9}	5×10^{-9}	10×10^{-9}	10×10^{-9}

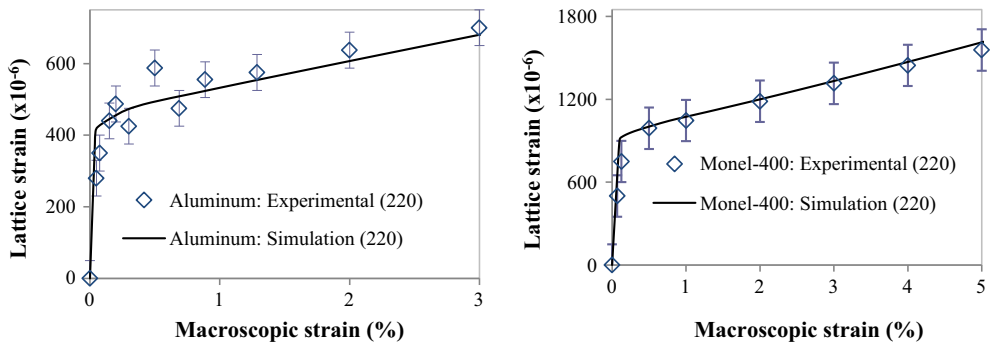

Fig. 4 Simulated and experimental elastic lattice strains for the 220 reflection for aluminium and MONEL-400

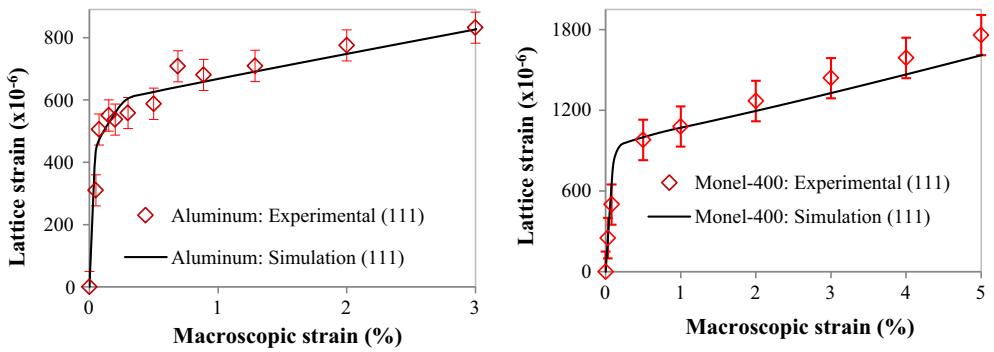

Fig. 5 Simulated and experimental elastic lattice strains for the 111 reflection for aluminium and MONEL-400

for a set of 1000 spherical inclusions. This number of crystallites has been chosen to simulate the polycrystalline aggregate in an efficient way.

The model parameters have been determined fitting the experimental macroscopic tensile curves plotted in Fig. 3. The parameter values are listed in Table 2. The predicted lattice strains are plotted in Figs. 4 and 5. The experimental data are also shown in these plots. The accuracy on the experimental lattice strains is about 10^{-4}.

Table 3 Chemical compositions of aluminium alloy 6060 and AISI 316L austenitic stainless steel

Si (%)			Fe (%)			Ng (%)			Ti (%)	
Aluminium alloy 6060										
0.46			0.19			0.47			0.01	
C (%)	Si (%)	Mn (%)	P (%)	S (%)	Cr (%)	Ni (%)	Mo (%)	Cu (%)	N (%)	Co (%)
AISI 316L austenitic stainless steel										
0.015	0.31	1.44	0.028	0.021	16.51	10.46	2.13	0.18	0.02	0.04

Figure 3 shows that the model enables a very accurate representation of the measured macroscopic stress–strain curves using the fitted parameters shown in Table 2. The relative deviation between experimental and simulation results is around 2 % for both materials. This is a first validation for the model on a macroscopic scale in monotonic loading for FCC structure.

In order to validate the model at mesoscopic scale, neutron diffraction has been used (Figs. 4, 5) for aluminium and MONEL-400 materials. The development of lattice strains is nonlinear once the specimen reaches the plastic regime. The model predicts this development on the elastic and plastic regimes. For the 220 reflection, the numerical predictions show a better agreement with experimental results. At 3 % macroscopic strain for aluminium, the relative deviation is 3 %. For MONEL-400, this deviation reaches 2 % at 5 % total strain. For the 111 reflection, the relative deviation is close to 0 % at 3 % macroscopic strain for aluminium but reaches 9 % at 5 % total strain for MONEL-400.

In a general way, the obtained results show that the model is able to predict the material behaviour at the mesoscopic and the macroscopic scales for FCC materials under monotonic loading.

In the next section, we will evaluate the ability of the model to simulate correctly the different physical aspects of the behaviour and the induced microstructure during uniaxial Bauschinger tests in tension–compression and compression–tension.

5.2 Prediction of Bauschinger effect

5.2.1 Materials and mechanical tests

The materials studied are an AISI 316L austenitic stainless steel and an aluminium alloy 6060. Their chemical compositions are detailed in Table 3. The specimens were cylindrical with a 20-mm diameter and a 140-mm length. Optical microscopy and scanning electron microscopy (SEM) experiments have been performed on the samples in order to reveal the grain size and morphology. Observations (not presented here) revealed an average grain size of 15 μm for the austenitic stainless steel and 90 μm for aluminium. The grain morphology study of two materials shows spherical forms.

For our simulations, the elastic single-crystal stiffness (GPa) for aluminium alloy 6060 (AISI 316L austenitic stainless steel) is as follows: $c_{11} = 104.54(248.35)$, $c_{12} = 59.22(99.35)$, $c_{44} = 25.88(70.43)$.

The initial residual stresses (longitudinal and transversal) were analysed in our laboratory with a four-circle XRD 3003 PTS SEIFERT goniometer using K_α chromium radiation and equipped with 0.5 mm diameter collimator. The diffraction peaks [(220) plane for austenitic stainless steel and (311) plane for aluminium alloy] were collected by a position-sensitive detector. Using Bragg's law, the interplanar spacing was calculated from diffraction peaks displacements for AISI 316L austenitic stainless steel. The modified $\sin^2\psi$ method for determining the stress field in anisotropic materials was used in order to study the stress evolution in our stainless steel sample. The initial residual stresses measured in our materials are negligible (around ± 10 MPa).

Several tension–compression and compression–tension tests with different pre-strains in tension (2, 4, 5, 6 and 10 % for AISI 316L austenitic stainless steel; and 2, 3, 4 and 5 % for aluminium 6060) were performed (Figs. 6, 7).

From experimental results (Figs. 6, 7), some remarks can be listed:

- For the first loading, the elastoplastic transient parts have a low radius of curvature as compared to the transient parts of the second one.
- During the reverse test, the transient part radius of curvature is important if the pre-strain is important.
- During the second loading, the stress values are higher than the first loading at the same strain.
- The yield strength for the second loading is lower than the first one.

These remarks agree with previous works [34].

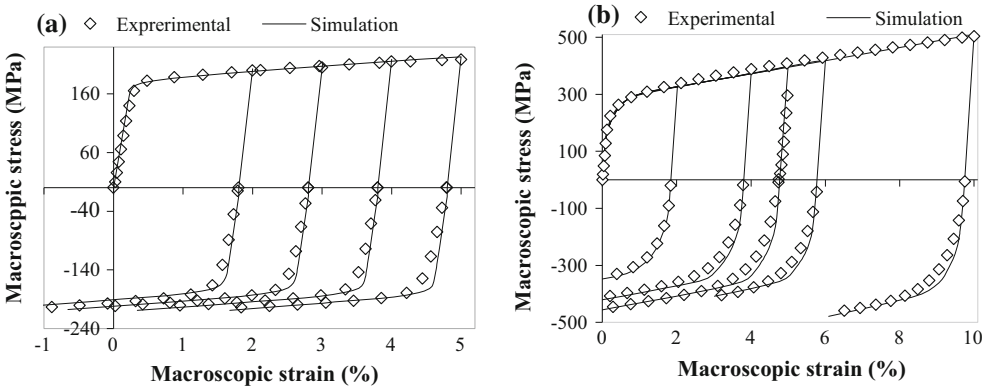

Fig. 6 Simulated and experimental stress–strain curves for aluminium alloy 6060 (**a**) and AISI 316L austenitic steel (**b**) during tensile–compression tests

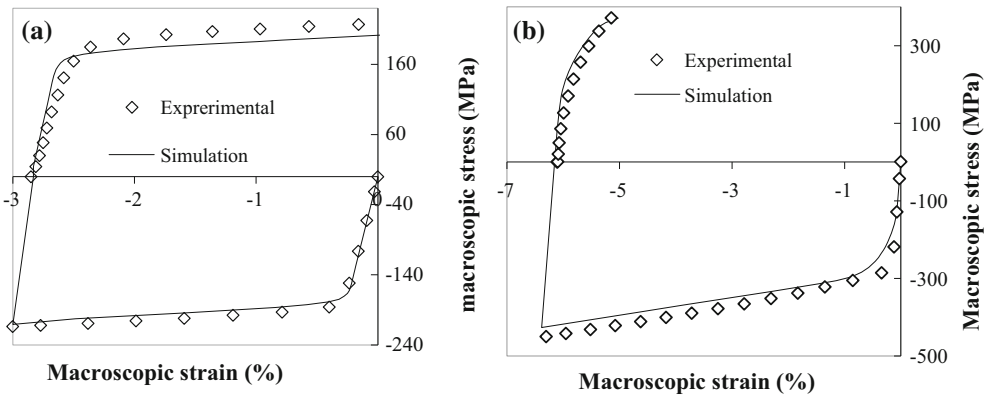

Fig. 7 Simulated and experimental stress–strain curves for aluminium alloy 6060 (**a**) and AISI 316L austenitic steel (**b**) during compression–traction tests

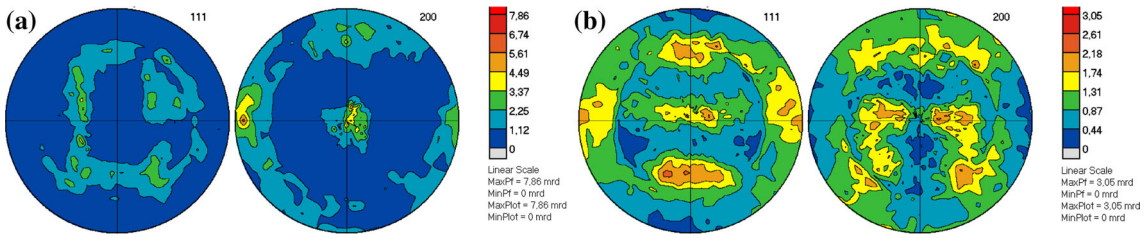

Fig. 8 Initial X-ray diffraction pole figures obtained on (200) and (111) diffracting planes of aluminium alloy 6060 (**a**) and AISI 316L austenitic steel (**b**)

5.2.2 Comparison between experimental and predicted results

The simulation results are compared to the experimental data (Figs. 6, 7). Texture measurements were analysed with a four-circle XRD 3003 PTS SEIFERT goniometer. $K\alpha$ copper radiation was used. The X-ray beam output collimator had a 0.5-mm diameter. The diffraction peaks were recorded with a position-sensitive detector. We have measured incomplete pole figures (PF) on a $5 \times 5°$ grid with tilt and azimuth angles ranging from 0 to 60° and 0 to 360°, respectively. For each experimental direction, the diffraction pattern has been adjusted using a nonlinear least-squares analysis and assuming pseudo-Voigt peak profiles in order to evaluate background noise and obtain peak intensities.

The orientation distribution function calculation was performed with experimental {111}, {220} and {200} pole figures with the help of the WIMV algorithm implemented in the BEARTEX program package [35] (Fig. 8).

Table 4 Parameters used for aluminium alloy 6060 and for AISI 316L austenitic stainless steel

τ_{c0} (MPa)	k	η	α	I	I^{wd}	I^{wp}	ρ_0 (m^{-2})	R (m)	R^{wd} (m)	R^{wp} (m)	R_{ncg} (m)	R_{rev} (m)	R_2 (m)
Aluminium alloy 6060													
72	0.5	100	0.1	0.1	0.3	0.1	10^{11}	8×10^{-9}	8×10^{-9}	8×10^{-9}	8×10^{-9}	11×10^{-9}	11×10^{-9}
AISI 316L austenitic stainless steel													
60	0.9	200	0.3	0.2	0.35	0.2	5×10^{9}	7×10^{-9}	7×10^{-9}	7×10^{-9}	7×10^{-9}	15×10^{-9}	15×10^{-9}

The initial texture is described by the three experimental Euler's angles. The model calculations were performed for a set of 1000 spherical inclusions. The material parameters (Table 4) have been determined fitting the experimental monotonic tensile curve (Figs. 7, 8). Whatever the material, a good correlation is obtained with the reference data. All experimental characteristics including the Bauschinger effect and the macroscopic work hardening are reproduced by the model for the tension–compression and compression–tension loadings at different pre-strain. For aluminium samples, the relative deviation of both results is between 0 and 10 %. For AISI 316L austenitic stainless steel, the relative deviation is around 8 %.

6 Conclusion

In this paper, a new approach has been developed in order to predict the elastoplastic behaviour of polycrystalline FCC materials under both monotonic and sequential loadings. This approach is based on a coupling between an intragranular description and a homogenization method. The dislocation density evolution is taken as an internal variable that can be set to one of the three following densities: the cell dislocation density, the immobile dislocations density and the directionally movable dislocation density. This description reproduces the softening and hardening phenomena observed during plasticity and allows to determine the grain behaviour. The meso–macro transition performed by an EPSC model is used to deduce the macroscopic behaviour of the polycrystal.

Different numerical results concerning the prediction of macroscopic and mesoscopic behaviour of polycrystal with FCC symmetry are presented, and a correct agreement is observed between the simulation data and the experimental results.

References

1. Liu, Q., Juul Jensen, D., Hansen, N.: Effect of grain orientation on deformation structure in cold-rolled polycrystalline aluminium. Acta Mater. **46**, 5819–5838 (1998). doi:10.1016/S1359-6454(98)00229-8
2. Ungar, T., Mughrabi, H., Rönnpagel, D., Wilkens, M.: X-ray line-broadening study of the dislocation cell structure in deformed [001]-orientated copper single crystals. Acta Metall. **32**, 333–342 (1984). doi:10.1016/0001-6160(84)90106-8
3. Borbely, A., Hoffmann, G., Aernoudt, E., Ungar, T.: Dislocation arrangement and residual long-range internal stresses in copper single crystals at large deformations. Acta Mater. **45**, 89–98 (1997)
4. Winther, G., Jensen, D.J.: Deformation induced dislocation boundaries: alignment and effect on mechanical properties. Comput. Mater. Sci. **9**, 251–260 (1997)
5. Boehler, J.-P., Khan, A.S.: Anisotropy and localization of plastic deformation. In: Proceedings of Plasticity '91 the Third International Symposium on Plasticity and Its Current Applications. Elsevier, New York (1991)
6. Chun, B.K., Jinn, J.T., Lee, J.K.: Modeling the Bauschinger effect for sheet metals, part I: theory. Int. J. Plast. **18**, 571–595 (2002). doi:10.1016/S0749-6419(01)00046-8
7. Bouvier, S., Alves, J.L., Oliveira, M.C., Menezes, L.F.: Modelling of anisotropic work-hardening behaviour of metallic materials subjected to strain-path changes. Comput. Mater. Sci. **32**, 301–315 (2005)
8. Kim, B.G., Dong, S.L., Park, S.D.: Effects of thermal processing on thermal expansion coefficient of a 50 vol.% SiCp/Al composite. Mater. Chem. Phys. **72**, 42–47 (2001)
9. Holden, T.M., Holt, R.A., Clarke, A.P.: Intergranular Stresses in Incoloy-800. Atomic Energy of Canada Limited, Chalk River, Ontario (1997)
10. Gloaguen, D., François, M., Guillen, R.: Mesoscopic residual stresses of plastic origin in zirconium: interpretation of X-ray diffraction results. J. Appl. Crystallogr. **37**, 934–940 (2004). doi:10.1107/S0021889804022034
11. Castelnau, O., Francillette, H., Bacroix, B., Lebensohn, R.A.: Texture dependent plastic behavior of Zr 702 at large strain. J. Nucl. Mater. **297**, 14–26 (2001)
12. Gloaguen, D., Francois, M., Guillen, R., Royer, J.: Evolution of internal stresses in rolled Zr702α. Acta Mater. **50**, 871–880 (2002)
13. Langlois, L., Berveiller, M.: Overall softening and anisotropy related with the formation and evolution of dislocation cell structures. Int. J. Plast. **19**, 599–624 (2003). doi:10.1016/S0749-6419(01)00074-2
14. Muller, D., Lemoine, X., Berveiller, M.: Nonlocal behavior of elastoplastic metals: theory and results. J. Eng. Mater. Technol. **116**, 378–383 (1994). doi:10.1115/1.2904301

15. Muller, D., Berveiller, M., Kratochvíl, J.: Non-local hardenings in metals. Mater. Sci. Forum **123**, 195–204 (1993). doi:10.4028/www.scientific.net/MSF.123-125.195
16. Mughrabi, H.: The long-range internal stress field in the dislocation wall structure of persistent slip bands. Phys. Status Solidi A **104**, 107–120 (1987). doi:10.1002/pssa.2211040108
17. Fajoui, J., Gloaguen, D., Courant, B., Guillén, R.: Micromechanical modelling of the elastoplastic behaviour of metallic material under strain-path changes. Comput. Mech. **44**, 285–296 (2009). doi:10.1007/s00466-009-0374-7
18. Peeters, B., Seefeldt, M., Teodosiu, C. et al.: Work-hardening/softening behaviour of b.c.c. polycrystals during changing strain paths: I An integrated model based on substructure and texture evolution, and its prediction of the stress–strain behaviour of an IF steel during two-stage strain paths. Acta Mater. **49**, 1607–1619 (2001). doi:10.1016/S1359-6454(01)00066-0
19. Karaman, I., Sehitoglu, H., Beaudoin, A.J. et al.: Modeling the deformation behavior of Hadfield steel single and polycrystals due to twinning and slip. Acta Mater. **48**, 2031–2047 (2000). doi:10.1016/S1359-6454(00)00051-3
20. Viatkina, E.M., Brekelmans, W.A.M., Geers, M.G.D.: Numerical analysis of strain path dependency in FCC metals. Comput. Mech. **41**, 391–405 (2008). doi:10.1007/s00466-007-0195-5
21. Peeters, B., Kalidindi, S.R., Teodosiu, C. et al.: A theoretical investigation of the influence of dislocation sheets on evolution of yield surfaces in single-phase B.C.C. polycrystals. J. Mech. Phys. Solids **50**, 783–807 (2002). doi:10.1016/S0022-5096(01)00094-1
22. Clausen, B., Lorentzen, T.: Experimental evaluation of a polycrystal deformation modeling scheme using neutron diffraction measurements. Metall. Mater. Trans. A **28**, 2537–2541 (1997). doi:10.1007/s11661-997-0011-z
23. Clausen, B., Lorentzen, T., Leffers, T.: Self-consistent modelling of the plastic deformation of F.C.C. polycrystals and its implications for diffraction measurements of internal stresses. Acta Mater. **46**, 3087–3098 (1998)
24. Mahesh, S., Tomé, C.N., McCabe, R.J. et al.: Application of a substructure-based hardening model to copper under loading path changes. Metall. Mater. Trans. A **35**, 3763–3774 (2004). doi:10.1007/s11661-004-0282-6
25. Franz, G., Abed-Meraim, F., Berveiller, M.: Strain localization analysis for single crystals and polycrystals: towards microstructure-ductility linkage. Int. J. Plast. **48**, 1–33 (2013). doi:10.1016/j.ijplas.2013.02.001
26. Franz, G., Abed-Meraim, F., Lorrain, J.-P. et al.: Ellipticity loss analysis for tangent moduli deduced from a large strain elastic–plastic self-consistent model. Int. J. Plast. **25**, 205–238 (2009). doi:10.1016/j.ijplas.2008.02.006
27. Fernandes, J.V., Schmitt, J.-H.: Dislocation microstructures in steel during deep drawing. Philos. Mag. Phys. Condens. Matter Defects Mech. Prop. **48**, 841–870 (1983)
28. Nesterova, E.V., Bacroix, B., Teodosiu, C.: Microstructure and texture evolution under strain-path changes in low-carbon interstitial-free steel. Metall. Mater. Trans. Phys. Metall. Mater. Sci. **32**, 2527–2538 (2001)
29. Feaugas, X.: On the origin of the tensile flow stress in the stainless steel AISI 316L at 300 K: back stress and effective stress. Acta Mater. **47**, 3617–3632 (1999). doi:10.1016/S1359-6454(99)00222-0
30. Kocks, U.F.: Texture and Anisotropy: Preferred Orientations in Polycrystals and Their Effect on Materials Properties. University Press, Cambridge (2000)
31. Lorrain, J.-P., Ben-Zineb, T., Abed-Meraim, F., Berveiller, M.: Ductility loss modelling for BCC single crystals. Int. J. Form. Process. **8**, 135–158 (2005). doi:10.3166/ijfp.8.135-158
32. Lipinski, P., Berveiller, M.: Elastoplasticity of micro-inhomogeneous metals at large strains. Int. J. Plast. **5**, 149–172 (1989). doi:10.1016/0749-6419(89)90027-2
33. Gloaguen, D., Berchi, T., Girard, E., Guillen, R.: Prediction of intergranular strains using a modified self-consistent elasto-plastic approach. Phys. Status Solidi Appl. Mater. Sci. **203**, 12–14 (2006)
34. Choteau, M., Quaegebeur, P., Degallaix, S.: Modelling of Bauschinger effect by various constitutive relations derived from thermodynamical formulation. Mech. Mater. **37**, 1143–1152 (2005). doi:10.1016/j.mechmat.2004.12.001
35. Wenk, H.-R., Matthies, S., Donovan, J., Chateigner, D.: BEARTEX: a Windows-based program system for quantitative texture analysis. J. Appl. Crystallogr. **31**, 262–269 (1998)